Understanding the intrinsic compression in polycrystalline films through a mean-field atomistic model

Enrique Vasco[1*], María J. Ramírez-Peral[1,2], Enrique G. Michel[2,3] and Celia Polop[2,3]

[1]*Instituto de Ciencia de Materiales de Madrid, CSIC, Sor Juana Inés de la Cruz 3, 28049 Madrid, Spain*

[2]*Departamento de Física de la Materia Condensada, Universidad Autónoma de Madrid, 28049 Madrid, Spain*

[3]*Condensed Matter Physics Center (IFIMAC), Universidad Autónoma de Madrid, 28049 Madrid, Spain*

(Dated: Jun. 25, 2020)

ABSTRACT

Recent advances on the nanoscale mapping of mechanical stresses on the surface of polycrystalline films have shed light on the origin of the intrinsic compression that appears recursively in these systems when the surface mobility is activated. This compression is identified with the Laplace pressure resulting from the adatom buildup at the edges of the gap where the grain boundaries emerge to the surface. Mesoscopic models of the surface evolution based on the Mullins-type diffusion numerically predict the existence of this accumulation of adatom. However, the physical mechanisms involved in this phenomenon has not yet been identified. Here, we interpret the phenomenon of mass accumulation at the edge of the grain-boundary gap in atomistic terms through a mean-field rate-equation model and demonstrate both its kinetic nature and its impact on the intrinsic stress of the system. Our results clarify the nanoscale physics underlying the Mullins´ Theory.

1. INTRODUCTION

The compact polycrystalline films show typically a latent compression state once the film is completed that is [1,2,3,4]: (a) regeneratable under high surface mobility conditions, and (b) thickness-independent. It might be described as a time bomb for applications and devices requiring a long lifespan and/or non-mild operating conditions. The accumulation of the regenerated intrinsic stress results in premature thermomechanical fatigue that underlies most mechanical failures. The origin of this behavior has been recently explained from a mean-field mesoscopic approach based on the Mullins´s theory [5,6]. It is due to the gradient of the surface chemical potential around the boundaries between the grains and coherent domains that form the polycrystalline solids. Among many other proposed explanations (which are not approached here [7]), this stands out for being the only one to date supported by direct measurements of mechanical stresses at the nanoscale, which is the characteristic spatial scale of the stress in solids [8]. However, an atomistic description of the physical mechanisms that underlies this explanation has not yet been provided. This description would help to account for the dependence of the intrinsic stress on the deposition parameters, in order to address the large set of experimental evidence reported so far.

In this work, we develop an atomistic model that sheds light on the physical processes involved in the mesoscopically described phenomenon [5,6]. In particular, we address the origin of the grain boundary (GB) surface profiles, which exhibit out-of-equilibrium shapes [8], characterized by mass buildup at the edges of the gap (or groove [9]) where the GBs emerge to the surface. The kinetic nature of the phenomenon is

probed and used to estimate the resulting profile of intrinsic stress in conditions of high atomic mobility.

1.1. Review of the mesoscopic Mullins´s theory

In this study, we assume a surface, which is initially in equilibrium, evolving under deposition conditions. As discussed earlier in Refs. [5,6], the equilibrium profile h_e in the vicinity of a GB counters the surface gradient of the balance $\vec{\nabla}_S\gamma$ between interfacial tensions along the GB gap profile (from the GB triple-junction to far-from-the-GB free surface). This causes the stress normal to the surface (i.e. $//\widehat{N}$) $\vec{\sigma}_N = -\vec{\nabla}_S\gamma\widehat{N}$, as described by the Laplace-Young equation, to be cancelled. The equilibrium profile $h_e(r)$, with r being the surface position, can be approximated by the expression [10]:

$$h_e(r) = 1.77h_{GB}ierfc[m_0(r - r_{GB})/1.77h_{GB}] \quad (1),$$

where h_{GB} denotes the GB triple-junction depth measured from the average height of the surface, $ierfc(x)$ corresponds to the integrate of the complementary error function, $m_0 = tan\{arcsin[\gamma_{GB}/2\gamma_s]\}$ is the equilibrium surface slope at the GB triple-junction, and r_{GB} is the GB position (r_{GB}=0 hereafter). The nature of the equilibrium profile $h_e(r)$ in Eq. 1 is discussed in Refs. [11,12,13].

Under deposition conditions far from equilibrium, the surface profile evolves according to the mesoscopic Mullins´s equation [10,13]

$$\frac{1}{\Omega}\partial_t h(r,t) = \vec{\nabla}_S\vec{J} \propto -\phi\nabla^4 h(r,t) \quad (2)$$

driven by a surface diffusion current $\vec{J} = -\phi\vec{\nabla}_s\kappa$. $\vec{J}$ is biased by the gradient of the surface curvature $\vec{\nabla}_s\kappa$ (driving force) where $\kappa \propto -\nabla^2 h$; ϕ, the diffusive mobility of

adatoms, corresponds to the kinetic constant of $\vec{J}$; and the minus sign considers the curvature sign convention [6]. Surface curvature provides an estimate of the surface chemical potential in terms of density of dangling bonds, $n_{db} \propto -\kappa$. Thus, $\vec{J}$ flows from the convex regions (where the density of dangling bonds is lower) towards concave ones (with higher density) through the flat areas.

Considering the surface slope constraint at the GB triple-junction and far from the GB (namely, $\partial_r h(r,t)|_{r\to r_{GB}} \to m_0$ and $\partial_r h(r,t)|_{r\to\infty} \to 0$, respectively) (see Fig. 6 of Ref. [6]), the solution of the Mullins´s equation causes the initial equilibrium profile to evolve into a kinetic state. This state is characterized by the mass accumulation at the edges on both sides of the GB gap [5,6,10]. In atomistic terms: (a) this mass accumulation can be understood as the buildup of adatoms with volume Ω, while (b) the slope constraint models the existence of local gradients in the density of steps between surface terraces. The physical mechanisms underlying mass accumulation are difficult to identify from the numerical solution of the mesoscopic model involving partial fourth order differential equation (Eq. 2). This fact, together with experimental difficulties in detecting the mass accumulations in steep regions close to the GB gaps by AFM, does not allow us a priori to rule out the existence of mathematical artifacts.

We inferred the following from the mesoscopic model, [5,6]: The law of conservation of mass (left part of Eq. 2) predicts that the accumulation must be induced by a non-null surface divergence $\vec{\nabla}_S$ of $\vec{J}$, which can be attributed to local changes in both the diffusive mobility ϕ of the adatoms (i.e., $\vec{\nabla}_S\phi \neq 0$) and/or the diffusion driving force $[\vec{\nabla}_S(\vec{\nabla}_S\kappa) \neq 0]$ along the GB gap profile:

$$\vec{\nabla}_S\vec{J} = -\vec{\nabla}_S\phi \cdot \vec{\nabla}_S k - \phi\vec{\nabla}_S(\vec{\nabla}_S k) \qquad (3).$$

In the case of the Mullins-type diffusive profile, the mass accumulation at the edges of the GB gaps has been ascribed to the decrease in the diffusive mobility of the adatoms as they diffuse towards the GB triple-junction. Plausibly, the diffusive mobility drops within the GB gap as the density of step-edge barriers to cross increases. This effect would reduce the interlayer transport, forcing the diffusing adatoms to meet each other and nucleate reversibly. On the other hand, although the surface curvature "diverges" at the GB triple-junction, causing the density of dangling bonds to reach a long-range maximum, the constriction of the surface slope limits the transport throughput (see the effective local rate of surface advance in Fig. 6 of Ref. [6]). This causes the gradient of superficial curvature to remain roughly constant ($\vec{\nabla}_S k \approx const.$) along the gap profile such that its divergence is minimized. In practical terms, the second term in Eq. 3 is much smaller than the first, and thus $\vec{\nabla}_S \vec{J} \propto -\vec{\nabla}_S \phi$.

In this context, a microscopic interpretation of the GB gap profile in terms of terraces and steps (vicinal surfaces), rather than the blind distribution of dangling bonds, helps us to identify the physical mechanisms involved in the phenomenon of mass accumulation induced by the Mullins-type diffusion on the surface of polycrystalline solids. As we know today [5,6,8], this phenomenon underlies the origin of the intrinsic stress experienced by these systems during their lifespan.

2. MODEL, RESULTS AND DISCUSSION

2.1. Atomistic approach to growth by step-flow

By applying the law of conservation of mass, the evolution of the surface profile (in Eq. 2) can be rewritten in atomistic parameters as:

$$\frac{1}{\Omega}\partial_t h(r,t) \propto F - \partial_t n_1(r,t) \quad (4),$$

where $n_1(r,t)$ is the density of diffusing monomers (i.e. single adatoms), which are deposited from a flux F and incorporated into the film bulk at the growth rate. Thus Eq. 4 distinguishes between the deposition rate F and the growth rate $\propto \partial_t h(r,t)$ through $n_1(r,t)$ evolution, which is described according the following kinetic rate equation:

$$\partial_t n_1 = F - D_s n_1 n_{step} - D_s[1-(\lambda/\xi)^2]n_1^2 + \beta D_s \nabla_s^2 n_1 \quad (5)$$

where D_s is the monomer diffusion coefficient, $n_{step} = \frac{3}{2}\left(\sqrt{2}/\partial_r h(r,t) - 3/4\right)^{-1}$ denotes the step density in a vicinal surface comprising fcc (111) terraces separated by indistinguishable A and B steps [14], λ/ξ corresponds to the diffusion length-to-grain size ratio, and β is a kinetic parameter described below. Since metal (111) planes with the highest close-packing and lowest energy cause the most of the polycrystalline metal films to grow [111]-textured with high roughness (following a Volmer-Weber mode), it makes sense to use a (111) vicinal surface as a generic growth scenario.

Eq. 5 corresponds to the easiest form of kinetic rate equation able to consider the following processes: The first term takes into consideration that the flux feeds evenly the monomer density; the second and third terms account for the decay in n_1 by monomer capture by steps and monomer capture by other monomers, respectively. The fourth term considers the monomer diffusion driven by surface gradients of n_1, which

corresponds to the thermodynamic potential involved in the Fick's first law $\vec{j}_1 = -D_s\vec{\nabla}n_1$. The capacity of the fourth term to homogenize spatially the monomer density is controlled by β. Eq. 5 assumes low growth temperatures, such that the re-evaporation is negligible.

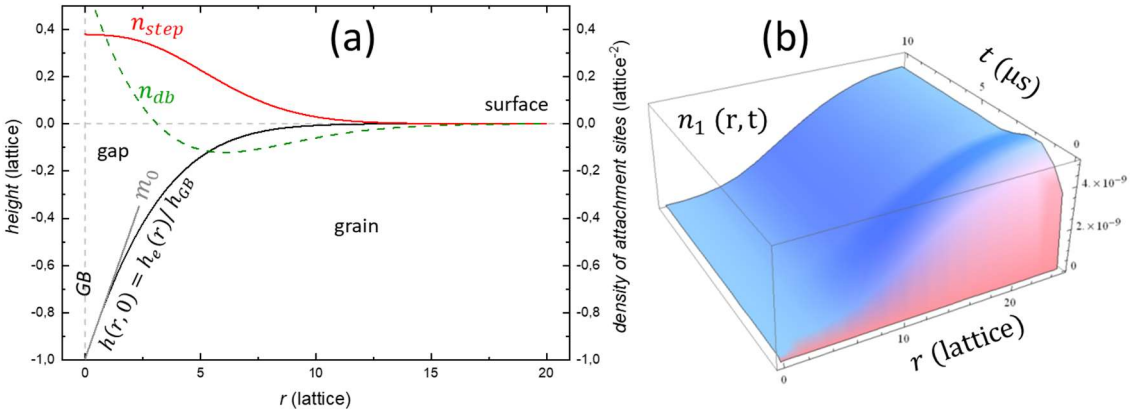

Fig. 1 **(a)** h_{GB}—normalized equilibrium surface profiles [$h(0) = h_e$, black curve] along with the density of A/B-undistinguishable (111) steps (n_{step}, red curve) and dangling bonds (n_{db}, dashed green curve) around a GB triple junction at r_{GB}=0 (with m_0=0.3 [15], gray line). **(b)** Evolution of the profile of the monomer density computed from Eq. 5 with F =0.5 nm/min, D_s=1.27×10^9 lattice^2/s [16] (D_s≈80 μm^2/s for Au with lattice parameter a =0.252 nm), $\beta = 0.01$ and $\xi = \lambda$ (i.e., kinetically limited growth by step-flow without second nucleation).

Fig. 1a displays the equilibrium profile (black curve) in the vicinity of a GB with m_0= 0.3 [15], along with its densities of (111) steps (n_{step}, red curve) and dangling bonds according to Mullins´s equation ($n_{db} \propto \nabla^2 h$, dashed green curve). As revealed from the n_{step} profile, the steps are concentrated within the GB gap. n_{step} remains nearly constant close to the GB triple-junction where the surface slope is constrained to m_0 (gray line) and decreases towards the grain surface. Note that the n_{step} profile differs greatly from the n_{db} profile, as considered by the Mullins´s theory [10] that predicts an accumulation of dangling bonds at the GB triple-junction where the surface curvature

diverges. Since in the polycrystalline films, the intrinsic stress relaxes (down to residual levels of two-three orders of magnitude lower) under low surface mobility conditions (e.g., at room conditions), the initial surface profiles (at $t = 0$) shown below are taken to be similar to h_{GB}-normalized equilibrium profiles [i.e., $h(r, t = 0) \equiv h_e(r)/h_{GB}$]. This is because major differences between initial and equilibrium profiles would imply high residual levels of stress (see discussed in section 2.2).

By replacing Eq. 5 in Eq. 4, the local rate of surface advance is described as follows:

$$\frac{1}{\Omega}\partial_t h = D_s n_1 n_{step} + D_s[1 - (\lambda/\xi)^2]n_1^2 - \beta D_s \nabla_s^2 n_1 \qquad (6).$$

The first term in Eq. 6 corresponds to growth by step-flow within the GB gap (i.e., steps capture diffusing monomers). The second term accounts for second nucleation on the grain top (diffusing monomers meet each other), and the third one correlates spatially the rates of the two first terms through the monomer density.

The factor $[1 - (\lambda/\xi)^2]$ in the second term evaluates the probability of second nucleation on the grain top. For grain sizes much larger than the diffusion length ($\xi \gg \lambda$), the contribution of the monomers to the step-flow is proportional to the number of atoms landing in the λ-wide strip near the GB (where n_{step} is higher), and then the monomer current is $j_1 \sim F\lambda(\lambda/\xi)$. Otherwise, all the deposited monomers contribute with $j_1 \sim F\xi$. In accordance with the law of conservation of mass, the probability of second nucleation can be estimated from the relative difference between these two cases $\propto [F\xi - F\lambda(\lambda/\xi)]/F\xi$. In principle, the diffusion length is effectively limited by the grain size, so that $[1 - (\lambda/\xi)^2]$ is ranged between 0 and 1 (i.e., without and with second nucleation, respectively).

On the other hand, the kinetic parameter β (in the third term of Eq. 6) ranges between two limiting cases: $\beta \approx 1$ corresponds to a kinetic limitation-free stage where the surface diffusion is much faster than the monomer capture and cancels any gradient of the monomer density. Otherwise, $\beta \ll 1$ corresponds to an aggregation-limited diffusion that characterizes kinetically limited growth. The interlayer transport delayed by step-edge barriers and/or reversible nucleation would be, potentially, the major kinetic limitations in these systems.

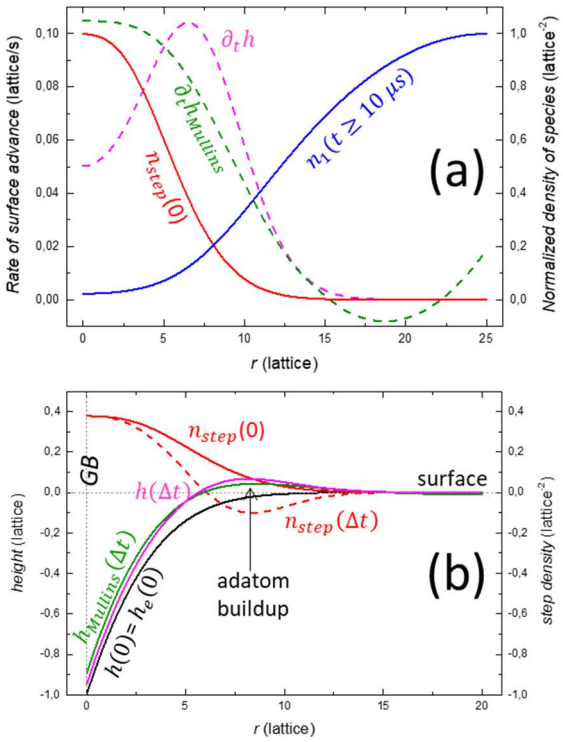

Fig. 2 (a) Profiles of: the steady monomer density (n_1, blue curve), the density of A/B-undistinguishable (111) steps (n_{step}, red curve), and the local rates of surface advance by step-flow ($\partial_t h$, dashed pink curve) and according to Mullins´s equation ($\partial_t h_{Mullins}$, dashed green curve) around a GB triple junction at $r = 0$ (with m_0=0.3, β=0.01 and $\xi = \lambda$). **(b)** Evolution of the surface profile (only one side is shown) after Δt =1 s growth by step-flow [compare the final profile (pink curve) with the numerical solution of Mullins´s equation (green curve), both obtained from the initial profile (black curve)]. The profiles of the densities of (111) steps before and after 1 s-growth (solid and dashed red curves, respectively) are included.

Fig. 1b shows the evolution of the n_1 profile computed by integrating Eq. 5 for a kinetically limited growth by step-flow (i.e., with $\beta = 0.01$ and $\xi = \lambda$). n_1 profile (along x-axis) stabilizes to steady values in fractions of μs (y-axis), which are different inside ($n_1 \to F/D_s n_{step}$) and outside ($n_1 \to \sqrt{F/D_s}$) the GB gap. These values differ in several orders of magnitude (~two orders in our study), which indicates that monomer density is depleted within the GB gap, in agreement with the predictions of the classical growth theories [17]. This result rules out previous models that attributed the postcoalescence compression to the insertion/trapping of adatoms in GBs [4,18,19] because since the GB gap is empty in monomers there is nothing to insert or capture. In this context, it is also interesting to note that Mullins´s theory predicted early that currents involving transport along GBs have a negligible effect on the material relaxation (see Eq. 15 in Ref. [10]).

(***Kinetically limited growth,*** $\boldsymbol{\beta \ll 1}$) Fig. 2a shows the local rate of surface advance by step-flow (first term in Eq. 6, $\partial_t h$ —dashed pink curve). The normalized profiles of densities of the involved species in this type of growth, namely, saturated n_1 (blue curve, for $t \geq$10 μs according to Fig. 1b) and initial n_{step} (red curve taken from Fig. 1a) are also included. Since both densities have opposite behaviors (n_1 rises as we move away from the GB while n_{step} drops), $\partial_t h$ exhibits a maximum where the product $n_1 \times n_{step}$ is highest. In other word, $\partial_t h$ is higher at the edge of the GB gap where both species coexist in moderate amounts. By way of comparison, the local rate of surface advance obtained from the slope-constrained Mullins´s equation ($\partial_t h_{Mullins}$ —dashed green curve taking from Fig. 6 of Ref. [6]) is also included in Fig. 2a. $\partial_t h_{Mullins}$ predicts higher growth within the gap, while $\partial_t h$ points to further accumulation on the edge. The

negative values of $\partial_t h_{Mullins}$ beyond the edge mean a depletion of the grain at long term, because unlike $\partial_t h$, $\partial_t h_{Mullins}$ does not correspond to an initial rate of surface advance.

Fig. 2b shows the surface profile that results from adding the local rates of surface advance ($\partial_t h$ and $\partial_t h_{Mullins}$, in Fig. 2a) for a given step time Δt (here Δt =1 s) to the initial profile [$h(0)$ —black curve] as: $h(r, \Delta t) \approx h(r, 0) + \Delta t \partial_t h(r, 0)$. The resulting microscopic profile [$h(\Delta t)$ —pink curve] shows a good agreement with the slope-constrained Mullins´s profile [$h(\Delta t)_{Mullins}$—green curve]. The accumulation of material at the edge of the GB gap, giving rise to ridges, is clearly visible in both profiles (see the arrowed volume), although this is smoother in the Mullins´s one.

The red curves display the evolution of n_{step} profile before (solid) and after (dashed) the surface advance. The accumulation of material at the edge results from the meet and nucleation of the adatoms along the diffusion path towards the GB triple junction. This gives rise to the formation of small terraces with unstable steps where the monomer capture is reversible. Consequently, n_{step} takes negative values to indicate that these sites correspond to delayed detachment sites (i.e., kinetic limitations as discussed above) rather than attachment sites.

(***Kinetic limitation-free growth, $\beta \to 1$***) Fig. 3a displays the β—dependence of n_1 for a step-flow regime. As β rises, the influence of the spatial distribution of the step density on the diffusion kinetics of the monomers decreases. The quick diffusion homogenizes spatially n_1 profile (along x-axis) in few μs (y-axis), as displayed in Figs. 3b. In the absence of major kinetic limitations (e.g. β=0.9), growth in regions with higher n_{step} prevails independently on the site positions/proximity. Consequently, the local rate of the

surface advance ($\partial_t h$ —dashed pink curve in Fig. 3c) reproduces well the shape of the normalized n_{step} profile (red curve in Fig. 3c). Note that both curves (dashed pink and red) exhibit a high degree of overlap.

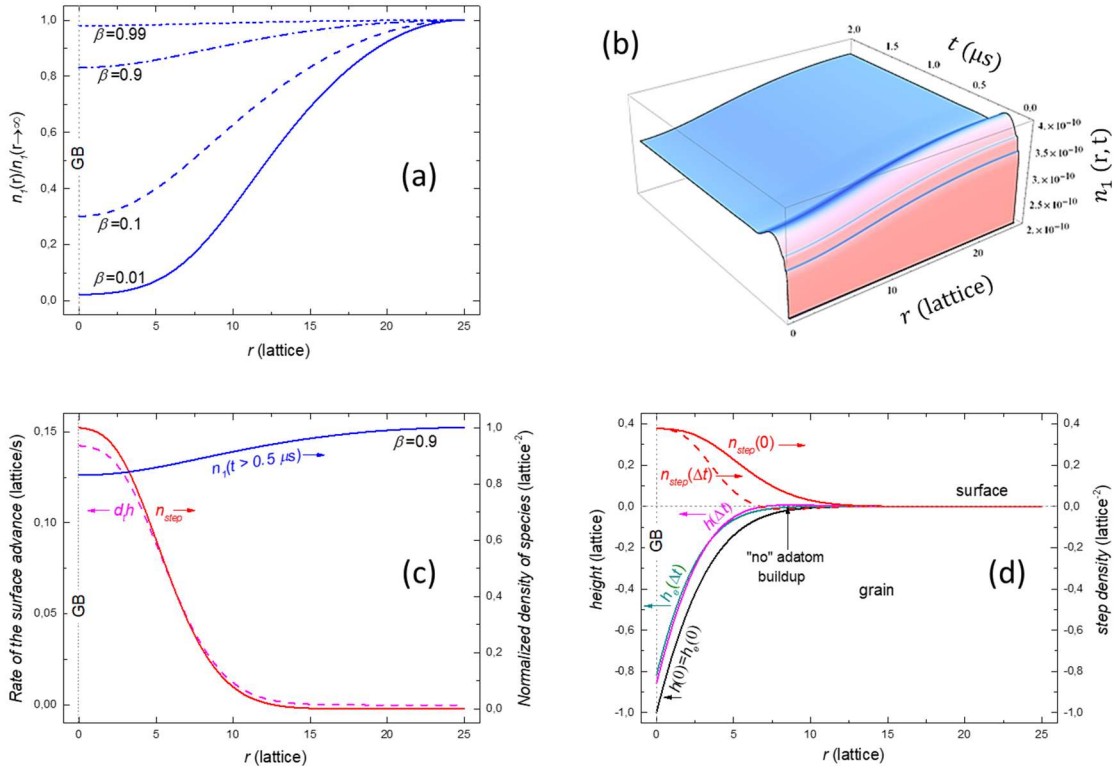

Fig. 3 (a) β—dependence of the n_1 profile around a GB triple junction at r =0 (with m_0=0.3 and $\xi = \lambda$) for growth by step-flow. n_1 profiles are normalized by their far-from-GB values (i.e., on the gain top). **(b, c and d)** Show similar results to those displayed in Fig. 1b, 2a and 2b, respectively, for the same set of parameters, except $\beta = 0.9$. Dark-cyan curve in (d) corresponds to the surface equilibrium profile for a similar deposited volume.

Fig. 3d shows the surface profile [$h(\Delta t)$ —pink curve] that results from the initial profile [$h(0)$ —black curve] considering the advance rate plotted in Fig. 3c after Δt =1 s of kinetic limitation-free growth by step-flow. The procedure is as the one followed to obtain the data plotted in Fig. 2b. However, the profile $h(\Delta t)$ that results in this case does not exhibit mass accumulation at the edge of the GB gap. On the contrary, a

comparison with the equilibrium profile [$h_e(\Delta t)$ —dark-cyan curve] corresponding to a similar deposited volume [20] reveals a good agreement between both. This agreement indicates that kinetic limitation-free growth does not modify the equilibrium condition between interfacial tensions (described by Laplace-Young equation) as expected.

At this point, we can provide a microscopic description of the surface kinetics underlying the phenomenon of mass accumulation at the edges of the GB gaps, which addresses the results of the mesoscopic model [6]. The adatoms diffuse from the grain tops towards the GB gaps where the density of dangling bonds is higher (this is the thermodynamic driving force of the process). However, their diffusive mobilities (that determinate the kinetics of the process, i.e., its rate) are limited by the reversible aggregation to the closer steps (where n_{step} is negative in Fig. 2b). In other words, while the long-range gradient of the density of steps biases the flow of diffusing adatoms, the short-range gradients control the flow rate and, consequently, the short-term surface advance.

2.2. Intrinsic Stress

Unlike the extrinsic stress in thin films, which is associated to lattice and thermal mismatches with the substrate, the intrinsic stress is attributed to unbalanced force fields that arise around discontinuities in the crystalline lattice of the films. In polycrystalline films, the lattices discontinuities playing major role in the generation of intrinsic stress are the grain boundaries and the film surface. As discussed above, the Laplace-Young equation describes the balance between these two discontinuities at the GB gap, with the Laplace pressure being the resulting stress for small perturbations in the equilibrium profile (Eq. 1). These perturbations must be understood in terms of changes

in the chemical potential of the surface, which is estimated from its curvature κ. Consequently, an intrinsic stress σ_N in the form of a Laplace pressure is generated:

$$\sigma_N(r,t)/\gamma_s = 2[\kappa_k(r,t) - \kappa_e(r,t)] \quad (7)$$

whenever the curvature κ_k of the surface profile that results from kinetically limited growth differs from the curvature κ_e of the surface profile that corresponds to kinetic limitation-free growth (that of equilibrium as demonstrated above), for a similar deposited volume.

Fig. 4 shows the surface profiles generated after Δt=1 s-deposition under kinetically limited and not limited conditions (pink and green curves, respectively), whose curvatures (dashed curves) differ from each other. The orange curve plots this difference $(\kappa_k - \kappa_e)$, which according Eq. 7, provides an estimate of the local ratio of the normal stress σ_N to the surface tension γ_s. For textured vicinal surfaces, formed by terraces with a preferential crystalline orientation, γ_s is roughly constant and then $\sigma_N(r,t) \propto (\kappa_k - \kappa_e)$. The thus-estimated stress profile exhibits an oscillatory behavior with a prevailing compressive contribution at the edge of GB gap (here around r ≈7.5 lattice from GB triple junction), which gives rise to a main compression averaged over the surface profile. From the data in Fig. 4, $\langle\sigma_N\rangle \approx 2\langle\kappa_k - \kappa_e\rangle\gamma_s \approx \left(\frac{2}{96.5}\right)\gamma_s/a \sim 2\%$ of γ_s/a, with a denoting the lattice parameter. The typical features (oscillating behavior, spatial range and local magnitude) of this stress profile agree reasonably with those measured experimentally in Au and Cu polycrystalline films by Atomic Force Microscopy-related techniques [8]. Besides, the estimate of the main compression in Fig. 4 from Au(111) parameters (γ_s ≈1.54 J/m^2 and $a = 0.252$ nm [21]) provides $\langle\sigma_N\rangle$ ≈123 MPa, which is within typical range of intrinsic stress jump reported for evaporated noble metals [19,22]. These results support the predictions of the models [3,5,6,23] that

attribute the generation of intrinsic stresses to the emerging of non-equilibrium structural shapes and profiles due to surface kinetics.

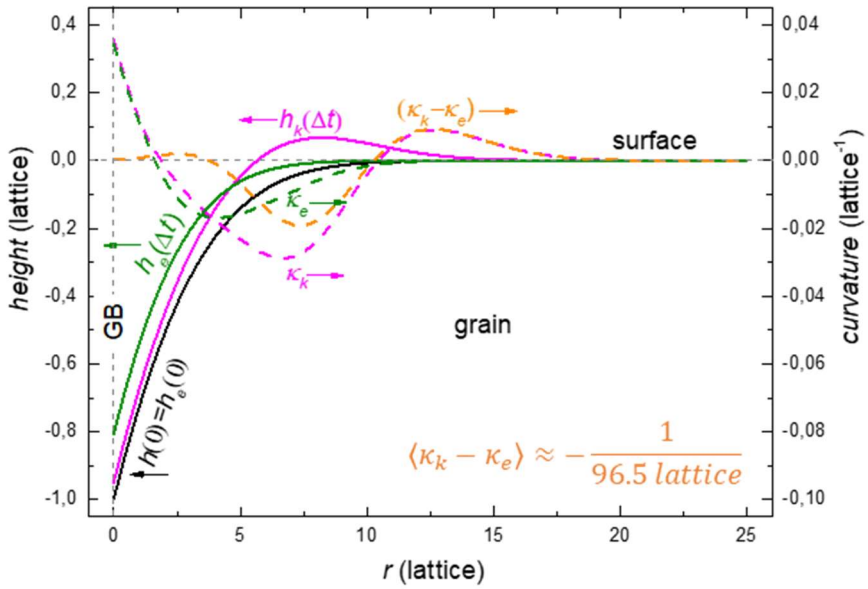

Fig. 4. Surface profiles (taken from Figs. 2b and 3d) resulting from kinetically limited (pink curve for β=0.01) and kinetic limitation-free (green curve for β=0.9) growths for the same deposited volume, together with their curvatures κ_k and κ_e (dashed curves of the same color), respectively. The difference between the curvatures $(\kappa_k - \kappa_e)$ is included (orange curve), together with its main value averaged over the surface profile.

2.3. Atomistic approach to growth by second nucleation

Since the diffusion length λ is determined by the diffusion coefficient-to-flux ratio, as $\lambda^6 \sim D_s/F$ for 2D+1 growth of films from diffusing monomers [13,17], the variation of the flux F and/or the deposition temperature T gives rise to diverse effects at different growth stages. During early growth stages of homogeneous nucleation and coalescence on substrates that do not prompt long-range order (e.g. substrates with amorphous surfaces or highly incommensurate ones), F (and complementary T) determines the average size of the grains $\xi \approx \lambda(\langle h\rangle \to 0)$, with $\langle h\rangle$ denoting the film thickness.

Otherwise, the *in-situ* variations of F and T (later growth parameters) during the postcoalescence modify the fraction of the grain surface $\lambda(\langle h\rangle \gg 0)/\xi$ involved in the phenomena of mass transport. As the flux increases and/or the temperature drops, the transport towards the GBs decreases and the step-flow leaves room for the second nucleation on the grain top for $\lambda \ll \xi$. The second nucleation on the same grain, which forces the crystalline coherence of the second nuclei, gives rise crystallites with slight misorientations to each other (in agreement with the Structure Zone Model´s predictions for zone 1b [24,25]), which coalesce without generating new grain boundaries. Instead, low-angle and CSL defects are formed. This behavior is similar to the case of seeded substrates. In short, changes in the later growth parameters (flux and/or temperature) induce extra roughness on the surface of the grains without significantly modifying their sizes. Consequently, later F (or T) and the average grain size (or the GB density) can be treated as independent growth parameters.

Based on the above considerations, the behavior of σ_N with the early growth parameters can be addressed straightforwardly from the dependence of the GB density on these parameters [26]. Thus for example, higher T_{early} (lower F_{early}) gives rise to larger grains, a lower density of GB sites between them, and consequently lower post-coalescence intrinsic compression. Conversely, the behavior of σ_N with the later growth parameters is more difficult to understand. On the other hand, dependence on intrinsic stress with flux characteristics that do not substantially alter surface diffusivity (e.g. its spatial inhomogeneity leading to shadowing, steering…) are not considered here. This is because intrinsic stress generation has also been observed in high surface mobility conditions that do not involve flux (e.g. by post-deposition annealing [15] and bombardment with energy particles [26]).

Figure 5a shows the λ/ξ—dependences of the densities of the surface species (monomers and steps) involved in film growth by (i) step-flow (with local rate of surface advance $\partial_t h \propto D_s n_1 n_{step}$ at the edge of grain-boundary), and (ii) second nucleation (with $\partial_t h \propto D_s[1-(\lambda/\xi)^2]n_1^2$ on the grain top). As λ/ξ decreases (from solid curve to increasingly dashed ones, according to arrows directions), the second nucleation prevails depleting the grain top of monomers. This is because the second nucleation implies the meet of several monomers, such that n_1 decays at a rate of $\partial_t n_1 \propto -n_1^2$. Fig. 5b shows the resulting surface profiles ($h(r,t)$ —pink curves, which are calculated in a similar way to those displayed in Figs. 2b and 3d), together with the corresponding equilibrium profiles [$h_e(r,t)$ —green curves]. Such equilibrium profiles are estimated by assuming: (a) a similar deposited volume [20], and (b) a similar height far from the grain boundary [i.e. $h_k(r\to\infty,t) \equiv h_e(r\to\infty,t)$]. The curvature curves (like those displayed in Fig. 4) are not included in Fig. 5b for the sake of clarity. Instead, their differences are plotted [$(\kappa_k - \kappa_e)$ —orange curves]. As λ/ξ decreases, the mass buildup on the edge of the grain-boundary gap is transferred to the grain top. This causes (not shown here—use Fig. 4 to follow the description) the minimum of curvature κ_k of the resulting surface profile to shift towards the GB position, while the minimum of κ_e is moving in the opposite direction. Thus, the curvature minima approach to each other, such that the overlap of the curvature curves results in a decrease in the minimum of their difference $(\kappa_k - \kappa_e)$, as shown in Fig. 5b. According to Eq. 7, this implies a decrease in both the compression maximum $max(\sigma_N)$ and its main value $\langle\sigma_N\rangle$.

Beyond the reported qualitative behavior of the intrinsic stress with the later deposition flux (namely, σ_N drops as F_{later} increases [27,28,29]), in this study, we aim to address the quantitative dependence between these two magnitudes. Fig. 5c shows

the λ/ξ—dependencies of $max(\sigma_N)/2\gamma_s$ and $\langle\sigma_N\rangle/2\gamma_s$ (red and black symbols, respectively), which fit well to parabolic functions (dashed curves). Assuming that the behavior of these statistical values is representative of the intrinsic stress, and taking into account $\lambda^6 \sim D_s/F$, we get:

$$\sigma_N \sim (\lambda/\xi)^2 \sim \left(F_{early}/F_{later}\right)^{2/6} \propto {F_{later}}^{-1/3} \quad (8),$$

where, as discussed above, $F_{early} = F(\langle h\rangle \to 0)$ is the early-growth flux, determining the grain size ξ. The power-law dependence $\sigma_N \propto {F_{later}}^{\alpha}$ (with $\alpha = -1/3$) in Eq. 8 is consistent with the later flux-dependences of the steady intrinsic stress σ_∞ reported for moderated fluxes and submicron-sized grains [27,28,29], whose power-law exponents are ranged between $\alpha = -0.21$ and -0.40 as displayed in Fig. 5d.

Eq. 8 describes the effects of the flux on intrinsic stress for different stages of growth. Thus, while the early increase in flux raises the density of grain boundaries around which the material under compression accumulates (i.e. σ_N increases), the late postcoalescence increase in flux induces extra surface roughness that results in traction between crystalline-coherent surface features (i.e. σ_N decreases [27]). However, the crossover between both regimes changes for 3D growths by Volmer-Weber mode owing to the kinetic roughening of the surface as the film grows [13]. Hence, early flux is not low enough to avoid second nucleation throughout deposition, and consequently late increases in flux are not necessary to induce extra-roughness and traction on grain surfaces. This effect may consistently explain the non-monotonic behavior of σ_N vs. flux (with a maximum of compression for intermediate fluxes) reported in Ref. [26].

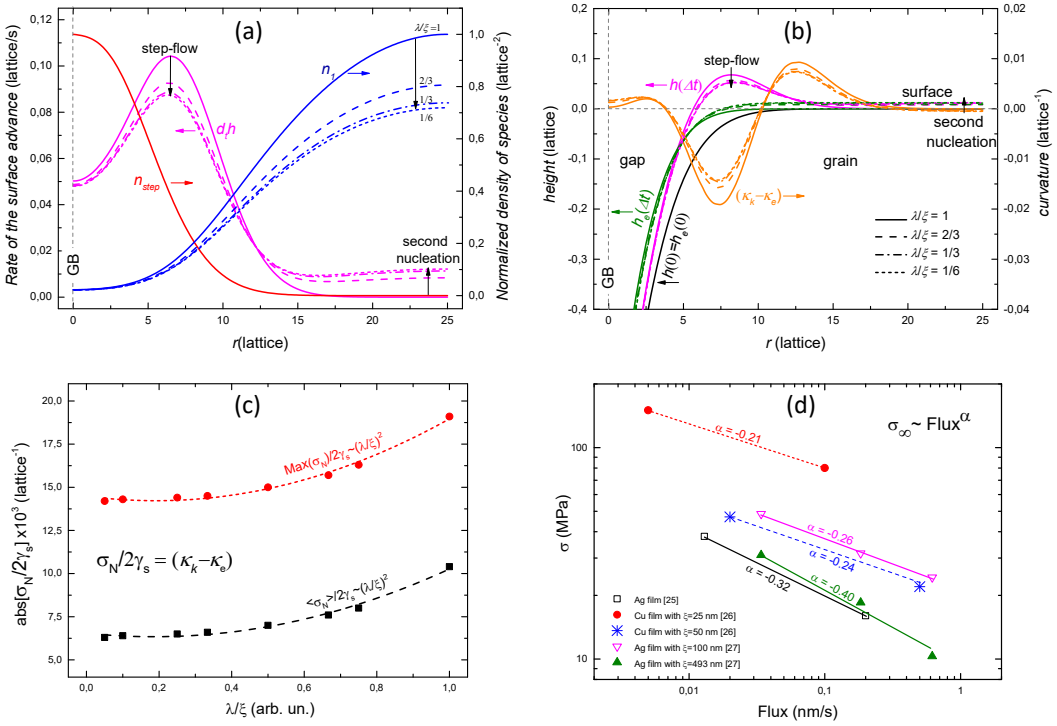

Fig. 5. λ/ξ—Dependence of: **(a)** the steady monomer density (n_1, blue curves), the density of A/B-undistinguishable (111) steps (n_{step}, red curve), and the local rates of surface advance ($\partial_t h$, pink curves). Vertical arrows indicate the direction of decrease in λ/ξ [from solid curve to increasingly dashed ones, as labelled in (a) and (b)]. **(b)** Surface profiles resulting from kinetically limited (pink curve for β=0.01) and kinetic limitation-free (green curve for β=0.9) growths for the same deposited volume, together the differences between their curvatures [$(\kappa_k - \kappa_e)$, orange curves]. The regions affected by step-flow and second nucleation are indicated in both figures. **(c)** λ/ξ—Dependences of $max(\sigma_N)/2\gamma_s = min(\kappa_k - \kappa_e)$ and $\langle\sigma_N\rangle/2\gamma_s = \langle\kappa_k - \kappa_e\rangle$ [red and black symbols computed from data in (b)] together their parabolic fits (dashed curves). **(d)** Fits of the data σ_N vs. F (where σ_∞ corresponds to the steady postcoalescence value of σ_N reported in the literature [27,28,29], see legend) to power-laws dependences.

3. CONCLUSIONS

An atomistic interpretation of the origin of the intrinsic stress in compact polycrystalline films is presented here. This interpretation supplements previous mesoscopic models (those in Refs. [5,6], and also the Mullins´s theory [10]) by shedding light on the growth mechanisms and the potential kinetic limitations involved. In short, the diffusion of monomers from grain surface to the GB gap, where the step density is higher, is kinetic limited by: (a) reversible aggregation to the nearest steps in the diffusion path and (b) nucleation via the meeting of monomers due to the decay in intralayer transport at the GB gap. These kinetic limitations give rise to non-equilibrium surface profiles, which, as we know today, are responsible for postcoalesce intrinsic compression. Compression, which as we have imaged by nanoscale stress mapping in Ref. [8], takes place at the edges of the GB gap rather than within the GB themselves. Once the growth mechanisms and kinetic limitations are identified, we are able to address/predict the dependence of the intrinsic stress with the deposition parameters (namely, the deposition flux and the growth temperature).

ACKNOWLEDGMENTS

This work was supported by the Ministerio de Economía, Industria y Competitividad (España) under Project No. FIS2017-82415-R; Ministerio de Ciencia, Innovación y Universidades (España) within the framework of UE M-ERA.NET 2018 program, under Project StressLIC (Spanish national subprojects PCI2019-103604 and PCI2019-103594).

REFERENCES

[1] J. A. Floro, S. J. Hearne, J. A. Hunter, P. Kotula, E. Chason, S. C. Seel, C. V. Thompson, The dynamic competition between stress generation and relaxation mechanisms during coalescence of Volmer–Weber thin films, J. Appl. Phys. 89 (2001) 4886-4897. https://doi.org/10.1063/1.1352563

[2] L. B. Freund, S. Suresh, Thin Film Materials —Stress, Defect Formation and Surface Evolution, Cambridge University Press, Cambridge UK, 2003.

[3] R. Koch, Dongzhi Hu, A. K. Das, Compressive Stress in Polycrystalline Volmer-Weber Films, Phys. Rev. Lett. 94 (2005) 146101. https://doi.org/10.1103/PhysRevLett.94.146101

[4] P. Jagtap, E. Chason, A unified Kinetic Model for stress relaxation and recovery during and after growth interruptions in polycrystalline thin films, Acta Mater. 193 (2020) 202-209. https://doi.org/10.1016/j.actamat.2020.04.013

[5] E. Vasco, C. Polop, Intrinsic Compressive Stress in Polycrystalline Films is Localized at Edges of the Grain Boundaries, Phys. Rev. Lett. 119 (2017) 256102. https://doi.org/10.1103/PhysRevLett.119.256102

[6] E. Vasco, E. G. Michel, C. Polop, Disclosing the origin of the postcoalescence compressive stress in polycrystalline films by nanoscale stress mapping, Phys. Rev. B 98 (2018) 195428. https://doi.org/10.1103/PhysRevB.98.195428

[7] Revise Refs. [3,4,6] for a detailed description and discussion of previous models, which mostly fail to bridge the gap between macroscopic stress measurements and the proposed atomistic mechanisms in the lack of information on the nanoscale stress field.

[8] C. Polop, E. Vasco, A. P. Perrino, R. Garcia, Mapping stress in polycrystals with sub-10 nm spatial resolution, Nanoscale 9 (2017) 13938-13946. https://doi.org/10.1039/c7nr00800g

[9] The terminology “GB gap” is used instead of groove to distinguish between pseudothermodynamic profiles (with small perturbations) and kinetic profiles (far from equilibrium). Note that Mullins [10] called “Grooving” to the evolution of the kinetic profiles towards the thermodynamic one.

[10] W. W. Mullins, Theory of Thermal Grooving, J. Appl. Phys. 28 (1957) 333-339. https://doi.org/10.1063/1.1722742

[11] In Ref. [10], Mullins assumes that both the vapor pressure and the chemical potential of a surface depend linearly on its local curvature for small-perturbation approximations to the Gibbs-Thompson formula. From these assumptions and the Edward-Wilkinson and Nernst-Einstein relations, Mullins determined the stationary surface profiles without and with diffusion within the vicinity of a grain boundary. The fact that these profiles are stabilized by the surface transport mechanisms against the kinetic roughening [12,13] and the thermodynamic nature of Gibbs-Thompson formula make the stationary profile without diffusion can be considered as an equilibrium profile.

[12] D. J. Srolovitz, On the stability of surfaces of stressed solids, Acta Metall. 37 (1989) 621-625. https://doi.org/10.1016/0001-6160(89)90246-0

[13] A. L. Barabási, H. E. Stanley, Fractal Concepts in Surface Growth, Cambridge University Press, Cambridge UK, 1995.

[14] A. González-González, J.L. Sacedón, C. Polop, E. Rodriguez-Cañas, J.A. Aznárez, E. Vasco, Surface slope distribution with mathematical molding on Au(111) thin film growth, J. Vac. Sci. Technol. A 27 (2009) 1012-1016. https://doi.org/10.1116/1.3130145

[15] Surface slope m_0=0.3 at the GB triple junction corresponds to a representative value taken within the measured range of border slopes in polycrystalline Au films by A. González-González, G.M. Alonzo-Medina, A.I. Oliva, C. Polop, J.L. Sacedón, and E. Vasco, Morphology evolution of thermally annealed polycrystalline thin films, Phys. Rev. B 84 (2011) 155450. https://doi.org/10.1103/PhysRevB.84.155450

[16] G. Antczak, G. Ehrlich, Surface Diffusion Metals, Metal Atoms, and Clusters, Cambridge University Press, Cambridge UK, 2010.

[17] T. Michely, J. Krug, Island, Mounds and Atoms: Patterns and Processes in Crystal Growth Far from Equilibrium, Springer-Verlag, Heidelberg Germany, 2004.

[18] H. Z. Yu, C. V. Thompson, Correlation of shape changes of grain surfaces and reversible stress evolution during interruptions of polycrystalline film growth, Appl. Phys. Lett. 104 (2014) 141913. https://doi.org/10.1063/1.4871214

[19] A. Saedi, M. J. Rost, Thermodynamics of deposition flux-dependent intrinsic film stress, Nat. Commun. 7 (2016) 10733. https://doi.org/10.1038/ncomms10733

[20] The equilibrium profile $h_e(\Delta t)$ for a deposited volume of $F\Delta t$ follows Eq. 1 from considering $h_{GB}(\Delta t)$ as a fitting parameter to fulfil the condition $\int_0^\infty [h_e(r,\Delta t) - h(r,0)]\partial r = F\Delta t$. Consequently, for the comparison in Fig. 3d: $\int_0^\infty [h_e(r,\Delta t) - h(r,0)]\partial r = \int_0^\infty [h(r,\Delta t) - h(r,0)]\partial r$.

[21] J. Mei, J. W. Davenport, G. W. Fernando, Analytic embedded-atom potentials for fcc metals: Application to liquid and solid copper, Phys. Rev. B 43 (1991) 4653-4658. https://doi.org/10.1103/PhysRevB.43.4653

[22] A.L. Shull, F. & Spaepen, Measurements of stress during vapor deposition of copper and silver thin films and multilayers, J. Appl. Phys. 80 (1996) 6243–6256. https://doi.org/10.1063/1.363701

[23] R. Abermann, R. Koch, The internal stress in thin silver, copper and gold films, Thin Solid Films 129 (1985) 71-78. https://doi.org/10.1016/0040-6090(85)90096-3

[24] C. R. M. Grovenor, H. T. G. Hentzell and D. A. Smith, The development of grain structure during growth of metallic films, Acta Metall. 32 (1984) 773. https://doi.org/10.1016/0001-6160(84)90150-0

[25] G. Timoshenko, Mechanics of Materials, PWS Publications, Boston USA, 1997

[26] A. Jamnig, N. Pliatsikas, K. Sarakinos, G. Abadias, The effect of kinetics on intrinsic stress generation and evolution in sputter-deposited films at conditions of high atomic mobility, J. Appl. Phys. 127 (2020) 045302. https://doi.org/10.1063/1.5130148

[27] E. Chason, B. W. Sheldon, L. B. Freund, J. A. Floro, and S. J. Hearne, Origin of Compressive Residual Stress in Polycrystalline Thin Films, Phys. Rev. Lett. 88 (2002) 156103. https://doi.org/10.1103/PhysRevLett.88.156103

[28] A. L. Del Vecchio, F. Spaepen, The effect of deposition rate on the intrinsic stress in copper and silver thin films, J. Appl. Phys. 101 (2007) 063518. https://doi.org/10.1063/1.2712150

[29] D. Flötotto, Z. M. Wang, L. P. H. Jeurgens, E. J. Mittemeijer, Kinetics and magnitude of the reversible stress evolution during polycrystalline film growth interruptions, J. Appl. Phys. 118, (2015) 055305. https://doi.org/10.1063/1.4928162